International Journal of Nanomedicine

Dovepress
Taylor & Francis Group

Open Access Full Text Article

ORIGINAL RESEARCH

ROS-Responsive Nano-Encapsulated Selenium Targeting Cervical Cancer Cell via PI3K/AKT Signaling Pathway

Yanmei Qiu[1,2,*], Chongke Hu[1,*], Sifang Zhao[3,*], Dezhi Chen[2], Jiaying Shen[1], Fanjia Dai[3], Mengxin Ban[3], Yimin Ma[3], Jingjing Weng[4], Xiaoping Huang[1], Yingying Zhu[4], Lingling Zhao[3], Fei Guo[1,2]

[1]Ningbo Institute of Innovation for Combined Medicine and Engineering (NIIME), The Affiliated LiHuili Hospital of Ningbo University, Ningbo, Zhejiang, 315100, People's Republic of China; [2]The First Affiliated Hospital, Jiangxi Medical College, Nanchang University, Nanchang, Jiangxi, 330006, People's Republic of China; [3]School of Materials Science and Chemical Engineering, Ningbo University, Ningbo, Zhejiang, 311215, People's Republic of China; [4]Department of Obstetrics and Gynecology, LiHuili Hospital Affiliated to Ningbo University, Ningbo, Zhejiang, 315040, People's Republic of China

*These authors contributed equally to this work

Correspondence: Fei Guo; Lingling Zhao, Email lhlguofei@nbu.edu.cn; zhaolingling@nbu.edu.cn

Purpose: Current cervical cancer treatments have yet to realize significant advances in patient quality of life. To overcome the challenges of off-target toxicity and inefficient delivery, we developed targeted ROS-responsive selenium nanoparticles, based on selenium's anticancer properties.

Methods: FA-ReRSeNPs were synthesized and subjected to systematic characterization of their physicochemical and biological properties. The anti-tumor activity of FA-ReRSeNPs, along with the mechanistic basis, was validated using integrated in vitro assays and in vivo animal models.

Results: Using human cervical cancer cells (Hela and SiHa) and a SiHa subcutaneous xenograft nude mouse model, we verified that FA-ReRSeNPs significantly reduced the selenium dose required for anticancer activity, while alleviating off-target damage to normal tissues. Mechanistic studies confirmed that FA-ReRSeNPs exert anticancer effects via inhibition of PI3K/AKT signaling pathway; this inhibition subsequently induces tumor cell apoptosis and restrains proliferation. Cross-validated results from in vitro assays and in vivo burden analyses demonstrate that FA-ReRSeNPs possess superior tumor-inhibitory potential with high targeting specificity.

Conclusion: This work confirms FA-ReRSeNPs as a precision-driven nanotherapeutic for cervical cancer management. The fusion of active targeting and ROS-responsive release mechanisms addresses the classic efficacy-toxicity dilemma of conventional anticancer agents, highlighting the translational value of intelligent nanoengineering in advancing cancer therapies.

Keywords: FA-ReRSeNPslenium, FA-ReRSeNPs, ROS-responsive delivery, cervical cancer, PI3K/AKT signaling pathway, targeted therapy

Introduction

Cervical cancer remains one of the leading causes of cancer-related mortality in women worldwide, with approximately 660,000 new cases and 350,000 deaths recorded globally in 2022.[1] Its prognosis varies substantially by region and access to care, with long-term survival rates particularly low among patients in resource-constrained settings.[2] Although HPV vaccines have revolutionized cervical cancer prevention, offering protection against the primary causal agent of the disease, global vaccine coverage remains inadequate,[3] leaving women in underserved areas, low- and middle-income countries, and regions without robust healthcare systems at persistently high risk of infection and disease progression.[4] Standard treatments (surgery, radiotherapy, chemotherapy) yield limited benefits for advanced cases, with a median progression-free survival of 17.5 months, and an overall response rate is below 50%.[5] Consequently, there is an urgent

https://doi.org/10.2147/IJN.S558115
Received: 27 August 2025
Accepted: 29 January 2026
Published: 7 February 2026

Graphical Abstract

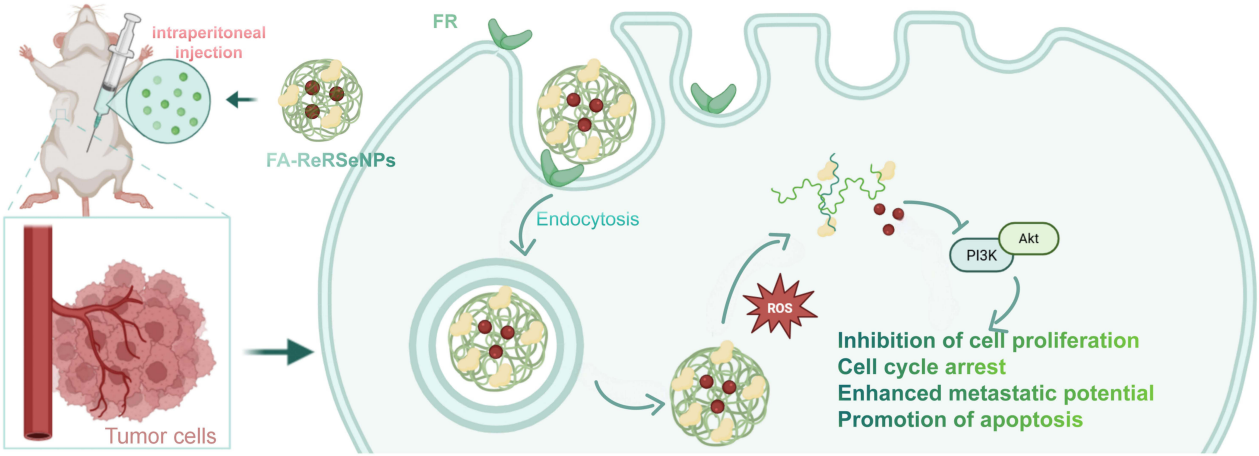

need to develop novel targeted therapies that offer high selectivity and low toxicity for better clinical management of cervical cancer.

Selenium, a trace element with distinctive reduction-oxidation (REDOX) properties, serves a dual role in cancer prevention and treatment.[6,7] Selenium serves as an essential micronutrient that supports the biosynthesis of selenoproteins, including glutathione peroxidase, a class of enzymes endowed with potent antioxidant activity that plays a pivotal role in preserving genomic integrity.[6,8] Conversely, at supra-physiological doses, selenium compounds (eg, selenite) exert pro-oxidative effects. These agents elevate reactive oxygen species (ROS) levels in tumor cells, subsequently triggering anti-tumor responses via mechanisms such as the induction of apoptotic cell death.[6,9–15] Our previous studies have demonstrated that selenium dioxide exhibits significant anticancer activity in cervical cancer models. This activity is linked to the regulation of epigenetic targets, including histone demethylases JMJD3 and UTX,[16] aligning with the established anticancer effects of selenium in liver cancer,[17] lung cancer,[18] and triple-negative breast cancer.[19] Yet, the clinical translation of selenium dioxide is greatly hampered by two key challenges: its lack of selective tumor-targeting capability and a relatively high risk of inducing systemic toxicity, both of which compromise its therapeutic safety and efficacy in vivo.

Given the unique physicochemical properties of selenium and the existing research base regarding its anticancer potential, addressing the clinical limitations of selenium dioxide, eg, as a direction for optimizing selenium-based anticancer strategies.[20] To this end, we proposed to design folate receptor (FR)-targeted and reactive oxygen species (ROS)-responsive selenium dioxide nanoparticles (FA-ReRSeNPs) to meet the needs of current selenium-based formulations.

The design logic is based on two well-documented characteristics of cervical cancer: first, folate receptor α (FR-α) is highly expressed in cervical cancer cells while being lowly expressed or absent in normal tissues[21–23] and this feature provides a molecular basis for active targeting delivery; second, the tumor microenvironment exhibits abnormally elevated ROS levels compared to normal tissues,[24–26] which enables the development of environment-responsive drug release systems.

Compared with phyco-synthesized Spirulina platensis selenium nanoparticles, which are characterized by favorable biocompatibility, surface active group-mediated stability, and multifunctional bioactivities (cytotoxicity against MCF-7 and SKOV-3 cancer cells), our folic acid-modified, ROS-responsive nanoplatform demonstrates distinct superiority in tumor-targeted drug delivery precision.[27] Encapsulating selenium dioxide (SeO_2) into a nano-carrier system with FR-targeting and ROS-responsive modules is expected to achieve two core objectives: enriching selenium at the tumor site

through FR-mediated targeting and realizing ROS-responsive drug-controlled release in the tumor microenvironment. This design is intended to retain the anticancer activity of selenium compounds while mitigating the non-specific systemic toxicity associated with free selenium dioxide, thereby laying a foundation for improving the therapeutic safety and accuracy of selenium-based cervical cancer therapy and promoting the clinical transformation potential of selenium-based drugs.

Materials and Methods

Cell Lines and Culture Medium

HeLa (C01-CA) human cervical adenocarcinoma cells and SiHa (C01-FH) human squamous carcinoma cells were obtained from Novobio (Shanghai, China) and cultured in DMEM and RPMI-1640 medium, respectively, supplemented with 10% fetal bovine serum (FBS, EVERY Green, Zhejiang, China). The cells were then incubated in a humidified environment at 37 °C with 5% CO_2.

Animals

Female BALB/C nude mice, aged 4 weeks, were procured from Hangzhou Muhao Biotechnology Co., Ltd. (Zhejiang, China) and were housed under standard sterile and specific pathogen-free (SPF) conditions. All animal experiments were conducted under the guidance of the Experimental Animal Welfare and Ethics Committee of the Ningbo Life and Health Industry Research Institute, Chinese Academy of Sciences (GK-2023-06-0001).

Synthesis of 1H-Imidazole-1-Carboxylic Acid, 4-(4,4,5,5-Tetramethyl-1,3,2-Dioxaborolan −2-Yl) Phenyl Methyl Ester (CDI-PBE)

CDI-PBE was synthesized according to a previous report.[28] Briefly, 468.2 mg PBE (2 mmol) was dissolved in 5 mL DCM, dehydrated by molecular sieve under stirring for 10 min at 25 °C. Then, 648.0 mg CDI (4 mmol) dissolved in 10 mL DCM was added slowly under stirring, and the mixture was reacted for another 24 h at 25 °C. The mixture was extracted three times with H_2O (3×10 mL), then extracted two times (2×10 mL) with saturated sodium chloride solution. The organic phase was collected and then dried with 100 mg anhydrous sodium sulfate for 30 min, and the white solid product was obtained after vacuum drying with a yield of 48.3%. Independent experimental repeats (n=3).

Synthesis of Phenylboric Acid Grafted GC (GC-PBA) and FA Modified GC-PBA (FA-GC-PBA)

GC-PBA was synthesized according to a previous report.[29] Briefly, 726.0 mg CDI-PBE (2.22 mmol) was dissolved in 25 mL DMSO, dehydrated by molecular sieve under stirring for 30 minutes at 25 °C. Then, 229.0 mg GC (1.11 mmol) and 298.0 mg DMAP (2.44 mmol) dissolved in 50 mL DMSO was added slowly under stirring, and the mixture was reacted for another 24 h at 25 °C. Then, the mixture was transferred into a dialysis tube (MWCO 8000–14000) and dialyzed against deionized water for three days with four changes every day. The residue was freeze-dried to obtain a white cotton-like product of GC-PBA with a yield of 47.4%. FA-GC-PBA was synthesized according to a previous report.[30] Briefly, 25.0 mg GC-PBA (2.22 mmol) was dissolved in 10 mL H_2O under stirring for 30 minutes at 25 °C. Then, 8.8 mg FA (0.02 mmol), 4.6 mg NHS (0.042 mmol), and 6.5 mg EDC·HCl (0.034 mmol) dissolved in 5 mL DMSO was added slowly under stirring. The mixture was reacted for another 24 h at 25 °C, and then transferred into a dialysis tube (MWCO 8000–14000) and dialyzed against deionized water for three days with four changes every day. The residue was freeze-dried to obtain a yellow cotton-like product of FA-GC-PBA with a yield of 81.3%.

Synthesis of RhB-Labeled FA-GC-PBA/GC-PBA (RhB-FA-GC-PBA/RhB-GC-PBA)

The synthesis of RhB-FA-GC-PBA/RhB-GC-PBA was carried out following a previously reported procedure.[31] First, 12.0 mg of RhB and 12.0 mg of FA - GC - PBA/GC - PBA were precisely weighed and separately dissolved in 2 mL of deionized water while being stirred at room temperature. After 30 minutes, the RhB solution was slowly added to the FA-GC-PBA/GC-PBA solution, and the mixture was continuously stirred at room temperature for 24 h. Subsequently, the

reaction mixture was dialyzed against deionized water using a dialysis membrane (MWCO 8000–14000) for 3 days, with the water being changed six times a day. Finally, the product was freeze-dried for 48 h to obtain RhB-FA-GC-PBA/RhB-GC-PBA.

Preparation of Selenite-Loaded Polymeric Nanoparticles

Selenite-loaded polymeric nanoparticles were synthesized according to a previous report.[32] Briefly, 12.0 mg FA-GC-PBA (0.1 mmol) was dissolved in 2 mL H_2O under stirring for 30 minutes at 25 °C. The pH of the solution was adjusted to 3.0 using 2 M sodium hydroxide solution. Subsequently, 12.0 mg of SeO_2 was dissolved in 2 mL of deionized water, where it dissociated to form selenous acid (H_2SeO_3) in the aqueous solution, which further ionized to generate Selenite anion (SeO_3^{2-}). The resulting SeO_3^{2-}-containing solution was then slowly added dropwise into the FA-GC-PBA solution. Under continuous stirring conditions, the SeO_3^{2-} bound to FA-GC-PBA molecules through electrostatic adsorption, and the reaction was allowed to proceed for 24 h at 25°C in the absence of light. Then, the mixture was transferred into a dialysis tube (MWCO 8000–14000) and dialyzed against deionized water for one day with six changes. The residue was freeze-dried to obtain a yellow cotton-like product with a yield of 53.6%. The content of Se in polymeric nanoparticles was measured using Inductively Coupled Plasma Optical Emission Spectrometry (ICP-OES) (SPECTRO, ARCOS). The drug loading efficiency (LE) and entrapment efficiency (EE) were calculated as follows:

$$LE = \frac{m_1}{m_2} * 100\%$$

$$EE = \frac{m_1}{m_3} * 100\%$$

Where m_1 is the content of Se in polymeric nanoparticles, m_2 is the total mass of selenite-loaded polymeric nanoparticles, and m_3 is the feed mass of SeO_2. The selenite-loaded FA-GC-PBA nanoparticles were labeled as FA-GC-PBA/SeO2.

Proton Nuclear Magnetic Resonance (^{1}H NMR) Spectrum

Proton nuclear magnetic resonance (1H NMR) spectra for all samples (GC-PBA, FA-GC-PBA, and FA-ReRSeNPs treated with reactive oxygen species) were acquired on a Bruker AVANCE III 400 MHz spectrometer. For preparation, each sample was weighed and dissolved in D_2O to yield a homogeneous solution at 5–10 mg/mL; tetramethylsilane (TMS) was added as an internal standard for chemical-shift calibration. Spectra were recorded with a spectral width of 12ppm, 64–256 scans (adjusted according to the sample signal-to-noise ratio), and a 2s relaxation delay. Free induction decay (FID) signals were Fourier-transformed using TopSpin, followed by baseline correction, chemical-shift calibration, and peak integration. Chemical shifts (δ) are reported in parts per million (ppm). Assignments of characteristic resonances were made by comparison with relevant literature and theoretical calculations and correlated with the samples' molecular structures.

Cell Viability Assay

The pharmacological effects of FA-ReRSeNPs on cell proliferation were evaluated using the Cell Counting Kit-8 (CCK-8, TransGen, Beijing, China) according to the manufacturer's instructions. HeLa and SiHa cells were seeded at a density of 1×10^4 cells/well in 96-well plates and treated with different concentrations of FA-ReRSeNPs for 48 h. After treatment, 100 μL of CCK-8 solution was added to each well, and the plates were incubated for an additional 2 h at 37 °C in a 5% CO_2 incubator. The optical density (OD) of each well was measured at 450 nm using a microplate reader (BioTek, VT, USA), and the data were graphically displayed. The growth rate (%) was calculated using the following formula: (OD experimental-OD blank)/(OD control-OD blank) × 100%. The Half Maximal Inhibitory Concentration (IC50) was determined using Graphpad Prism 9 software (Graphpad Software, USA). Independent experimental repeats (n=3).

Internal Uptake Assay

SiHa and HeLa cells in logarithmic growth phase were seeded at a density of 5×10^4 cells/well in 24-well confocal plates. Following cell adhesion, cultures were divided into three experimental groups: Phosphate-Buffered Saline (PBS) control,

FA-ReRSeNPs treatment, and FA-ReRSeNPs + folic acid co-treatment. Cells were incubated with FA-ReRSeNPs (1.3 μg/mL for HeLa, 2.6 μg/mL for SiHa) and FA (2 mM) in a 37°C humidified incubator for 4 h. After incubation, the medium was aspirated, and cells were washed thrice with serum-free medium. Nuclei of viable cells were then stained with Hoechst 33342 for 10 minutes, followed by three additional washes. Prior to imaging, anti-fade mounting medium was applied, and cellular internalization was visualized using confocal laser scanning microscopy. Independent experimental repeats (n=3).

Colony Formation Assay

HeLa and SiHa cells were plated in 6-well culture plates at a density of 1000 cells/mL. Following adherence in complete medium, the FA-ReRSeNPs treatment group received fresh medium containing FA-ReRSeNPs (1.3 μg/mL for HeLa, 2.6 μg/mL for SiHa), while the control group was replenished with complete medium alone. Medium was refreshed every 72 h. After 10–14 days of culture, cells were gently washed with PBS, fixed with 4% paraformaldehyde for 15 min, and stained with 0.1% crystal violet solution for 20 min. Colonies exceeding 50 μm in diameter were quantified and statistically analyzed using ImageJ software. Independent experimental repeats (n=3).

Western Blot

After treating SiHa and HeLa cells, the supernatant was removed and prechilled RIPA lysis buffer containing protease and phosphatase inhibitors was added. Cells were lysed on ice for 5 minutes, and lysates were transferred to sterile 1.5 mL microcentrifuge tubes. For subcutaneous xenograft tumor tissues, prechilled RIPA lysis buffer with protease and phosphatase inhibitors was added at a ratio of 1:9 (m/v). Tissue was homogenized thoroughly on ice and the homogenate transferred to sterile 1.5 mL microcentrifuge tubes. Samples were lysed on ice for 30 minutes, then centrifuged at 12000 × g for 15 minutes at 4°C. The supernatant was transferred to fresh tubes. Protein concentration was determined by the BCA assay (BSA standard) measuring absorbance at 562 nm. Five-times SDS loading buffer was added to the protein supernatant, and samples were boiled at 100°C for 10 minutes to denature proteins. After denaturation, aliquots were stored at −80°C until use. Prepare SDS-PAGE gels using 10–12% separating gels (NCM Biotech, Cat. No. P2012/P2013, China). Combine samples with 5× loading buffer and load them onto the gel alongside a protein marker (Abclonal, Cat. No. RM19001, China; Servicebio, Cat. No. G2087-250UL, China) for reference. Run electrophoresis on a Baygenebiotech BG-verMIDI system (China), applying 80 V for the stacking gel and 120 V for the separating gel. Transfer proteins to a PVDF membrane (Millipore, Cat. No. IPVH0010, China) using the wet-transfer method. The membrane was blocked at room temperature for 1 hour with Tris-buffered saline containing 5% skim milk and Tween® 20 (TBST; Servicebio, Cat. No. G0004-1L, China). The primary antibody, diluted 1:1000, was applied and the membrane incubated overnight at 4°C. After three 10-minute washes with TBST, an HRP-conjugated secondary antibody diluted 1:5000 was added and the membrane incubated at room temperature for 1 hour. After a final wash with TBST, protein bands were developed using enhanced chemiluminescence (ECL) substrate (NCM biotech, Cat. No. P10100, China) and imaged with a chemiluminescence imaging system. Band intensities were quantified with ImageJ (National Institutes of Health, NIH, USA), and statistical analyses were performed in GraphPad Prism 9.5.0 (GraphPad Software, USA). Data are presented as mean ± standard error of the mean (mean ± SEM) from at least three independent experiments; experiments were independently repeated three times (n = 3).

Flow Cytometry Assay

To assess cell cycle distribution and apoptosis, 7×10^4 cells were seeded in 6-well plates and treated with FA-ReRSeNPs (1.3 μg/mL for HeLa cells, 2.6 μg/mL for SiHa cells). Samples for cell cycle analysis were stained with propidium iodide (BD Biosciences, MA, USA), and samples for apoptosis analysis were stained with Annexin V-FITC and propidium iodide (TransGen, Beijing, China). Flow cytometry was performed using a BD FACSCanto II™ flow cytometer (BD Biosciences, MA, USA). Cell cycle distribution was analyzed using ModFit LT V3.1 (Verity Software House, USA) software, and apoptosis was analyzed using FlowJo V10.0.7 (Treestar Inc., Ashland, OR, USA) software. Independent experimental repeats (n=3).

Scratch Wound Healing Assay

Cells were seeded in 24-well plates and treated with FA-ReRSeNPs (1.3 μg/mL for HeLa cells, 2.6 μg/mL for SiHa cells) or PBS solvent control. Before treatment, a clean line was created using a sterile 200 μL pipette tip. Cell migration was observed under an inverted microscope (Leica DMI 6000 B, GER), and images were taken at 0 h and 48 h. The relative scratch area was calculated using ImageJ software. The wound healing percentage (%) was calculated using the formula: 1 - (S48 h / S0 h) × 100%, where S0 h represents the initial scratch area at 0 h, and S48 h represents the scratch area at 48 h. Independent experimental repeats (n=3).

Transwell Assay

Polycarbonate membrane Transwell chambers (8.0 μm pore size; Corning, USA) were placed in 24-well culture plates. For migration assays, HeLa cells (5×10^4/well) and SiHa cells (3×10^4/well) were seeded in the upper chamber with 200 μL serum-free medium containing FA-ReRSeNPs (1.3 μg/mL for HeLa, 2.6 μg/mL for SiHa) or PBS control. For invasion assays, the upper chamber was pre-coated with 100 μL Matrigel (Corning, USA) diluted 1:8 in serum-free medium, with other steps identical to migration assays. The lower chamber contained 800μL complete medium with 10% FBS as a chemoattractant. After incubation at 37°C with 5% CO_2, non-migrated/invaded cells on the upper membrane surface were removed with cotton swabs. Trans-membranous cells were fixed with 4% paraformaldehyde for 30 minutes, stained with 0.1% crystal violet, and quantified under high-power microscopy (200× magnification) by counting five random non-overlapping fields per membrane. Independent experimental repeats (n=3).

Reactive Oxygen Species (ROS) Detection

SiHa and HeLa cells in the logarithmic growth phase were seeded into 24-well confocal plates at a density of 5×10^4 cells per well. After cell adhesion, they were divided into the PBS group and the FA-ReRSeNPs group. Following 48 h treatment with FA-ReRSeNPs (1.3 μg/mL for HeLa cells, 2.6 μg/mL for SiHa cells), intracellular ROS were detected using 2',7'-dichlorodihydrofluorescein diacetate (DCFH-DA: D6470, Solarbio, China). DCFH-DA was diluted with serum-free medium at a ratio of 1:1000 to a final concentration of 10 μmol/L. The cell culture medium was removed, and an appropriate volume of diluted DCFH-DA was added. The cells were incubated in a 37°C cell culture incubator for 20 minutes, washed three times with serum-free medium, and then the nuclei of viable cells were stained with Hoechst 33342 (B8040, Solarbio, China). After washing the cells three times with serum-free medium, an anti-quenching agent was added, and the cells were observed under a confocal microscope. Independent experimental repeats (n=3).

RNA-Seq Analysis

SiHa cells in the logarithmic growth phase were evenly divided into PBS and SeO_2 groups. The PBS group was treated with PBS buffer as a control, while the SeO_2 group was treated with filter-sterilized selenium dioxide dissolved in PBS to reach the predetermined experimental concentration for 48 h. After treatment, cells were washed with ice-cold PBS, and total Ribonucleic Acid (RNA) was extracted using an RNA extraction kit. RNA concentration and purity were measured using a NanoDrop spectrophotometer, and integrity was verified by agarose gel electrophoresis. Qualified RNA samples were sent to Novogene Co., Ltd. (Beijing, China) for library preparation and sequencing. Raw sequencing data were processed to obtain clean reads, which were then aligned to the human reference genome using Hisat2. Gene expression levels were quantified using FeatureCounts, and differentially expressed genes (DEGs) were identified using DESeq2 (screening criteria: $|\log_2 FC| \geq 1$ and adjusted $P< 0.05$). Functional enrichment analysis of DEGs was performed for Gene Ontology (GO) terms and KEGG pathways.

Subcutaneous Xenograft Model

Female BALB/C nude mice were obtained from Hangzhou Zhemu Biotechnology Co., Ltd. (Hangzhou, China) for the xenograft mouse model. Mice were acclimatized to the laboratory environment for 1 week before the experiment and provided with free access to food and water. SiHa cells (5×10^6) were injected into the right upper limb of mice at

a volume of 200 μL to establish tumor-bearing BALB/c nude mice. On the 7th day post tumor cell injection, mice were randomly assigned to three groups: sham operation, empty vector, and FA-ReRSeNPs treatment. The treatment group received intraperitoneal injections of FA-ReRSeNPs at a dosage of 1.5 mg/kg (200 μL per mouse). The sham operation group received equivalent injections of PBS, while the empty vector group received injections of a selenium-free vector. Each group consisted of 7 mice, with all injections administered once every two days. These injections were administered every 2 days. Tumor length (L) and width (W) were measured every 2 days using calipers, and tumor volume was calculated using the formula $(L \times W^2)/2$. On day 18 post-treatment, euthanasia was performed in strict accordance with the American Veterinary Medical Association (AVMA) 2020 Guidelines. Prior to the procedure, mice were anesthetized with 5% isoflurane (RWD) to minimize pain. Adequate anesthesia was confirmed by monitoring corneal reflex and respiratory rate. Following confirmation, mice were euthanized by cervical dislocation. All personnel were specially trained in the technique and wore disposable sterile gloves to prevent cross-contamination. The atlanto-occipital junction was identified precisely as the site for dislocation. During the procedure, the non-dominant hand securely stabilized the mouse's head (from behind the ears to the orbital region) and back, while the dominant hand grasped the base of the tail and swiftly pulled in the opposite direction with a slight twist of the head, achieving dislocation within one second (a distinct "click" was audible). Following dislocation, the mouse was monitored until the absence of spontaneous breathing and limb convulsions for over 5 minutes confirmed death. All tumor tissues were subsequently collected for further analysis.

Statistical Analysis

The data are presented as mean±standard deviation (mean±SD), and all graphs and statistical analyses were performed using GraphPad Prism 9 software. Unpaired/Paired Student's *t*-test or one-way ANOVA was used to compare statistical differences between groups. A P-value < 0.05 was considered statistically significant (ns, $P>0.05$, *$P<0.05$, **$P<0.01$, ***$P<0.001$, ****$P<0.0001$).

Results

Synthesis, Validation, and Stability of FA-ReRSeNPs

Figure 1A illustrates the synthetic route for FA-ReRSeNPs. Initially, 1H-imidazole-1-carboxylic acid, 4-(4,4,5,5-tetramethyl-1,3,2-dioxaborolan-2-yl) phenyl methyl ester (CDI-PBE) was synthesized and grafted onto glycylchitosan (GC) amino groups via ammonolysis. Subsequently, boronate ester hydrolysis was performed to conjugate the phenylboronic acid moiety to the GC backbone. Then, folic acid (FA) was conjugated to GC as a targeting ligand. Finally, selenium dioxide was dissolved in deionized water to form a selenious acid solution, where selenite ions electrostatically adsorbed onto FA-GC-PBA to form FA-GC-PBA/SeO_2 (FA-ReRSeNPs). The successful synthesis of GC-PBA and FA-GC-PBA was confirmed by ^{1}H NMR. GC-PBA exhibited a broad peak at 3.0–3.9 ppm (GC protons),[33] as shown in Figure 1B. Resonances at 7.2/7.6 ppm (phenylboronic acid aromatic protons) and 6.7 ppm (methylene protons) confirmed PBA conjugation. FA-GC-PBA showed additional peaks at 6.65, 7.65, and 8.65 ppm, assigned to folic acid's pteridine ring,[30] verifying FA attachment. Observation of the appearance changes of the sample suspension system revealed that GC-PBA formed a brown turbid suspension in phosphate-buffered saline (PBS) within 48h, and the suspension gradually became clear after treatment with 1 mM hydrogen peroxide (H_2O_2) (Figure 1C). Further ^{1}H NMR analysis was performed on GC-PBA after H_2O_2 treatment (Figure 1D), and the results showed that the characteristic peaks at chemical shifts of 7.2 ppm and 7.6 ppm, assigned to the protons of the aromatic ring in PBA, completely disappeared. The aforementioned changes in appearance and NMR spectra collectively confirmed that the phenylboronic acid moiety was removed under H_2O_2 treatment as expected, verifying that GC-PBA possesses reliable reactive oxygen species (ROS)-responsive properties. FA-GC-PBA self-assembled into nanoparticles (227.8 ± 3.0 nm by DLS; Figure 1E) in aqueous solution. The selenium content of FA-ReRSeNPs was quantified at 25 mg/kg as measured by inductively coupled plasma emission spectroscopy. Stability assays in PBS (37°C) revealed negligible particle size fluctuations throughout incubation (Figure 1F), demonstrating robust colloidal stability. Transmission electron microscopy (TEM) further confirmed the formation of FA-GC-PBA/SeO_2 nanoparticles (Figure 1G).

 https://doi.org/10.2147/IJN.S558115

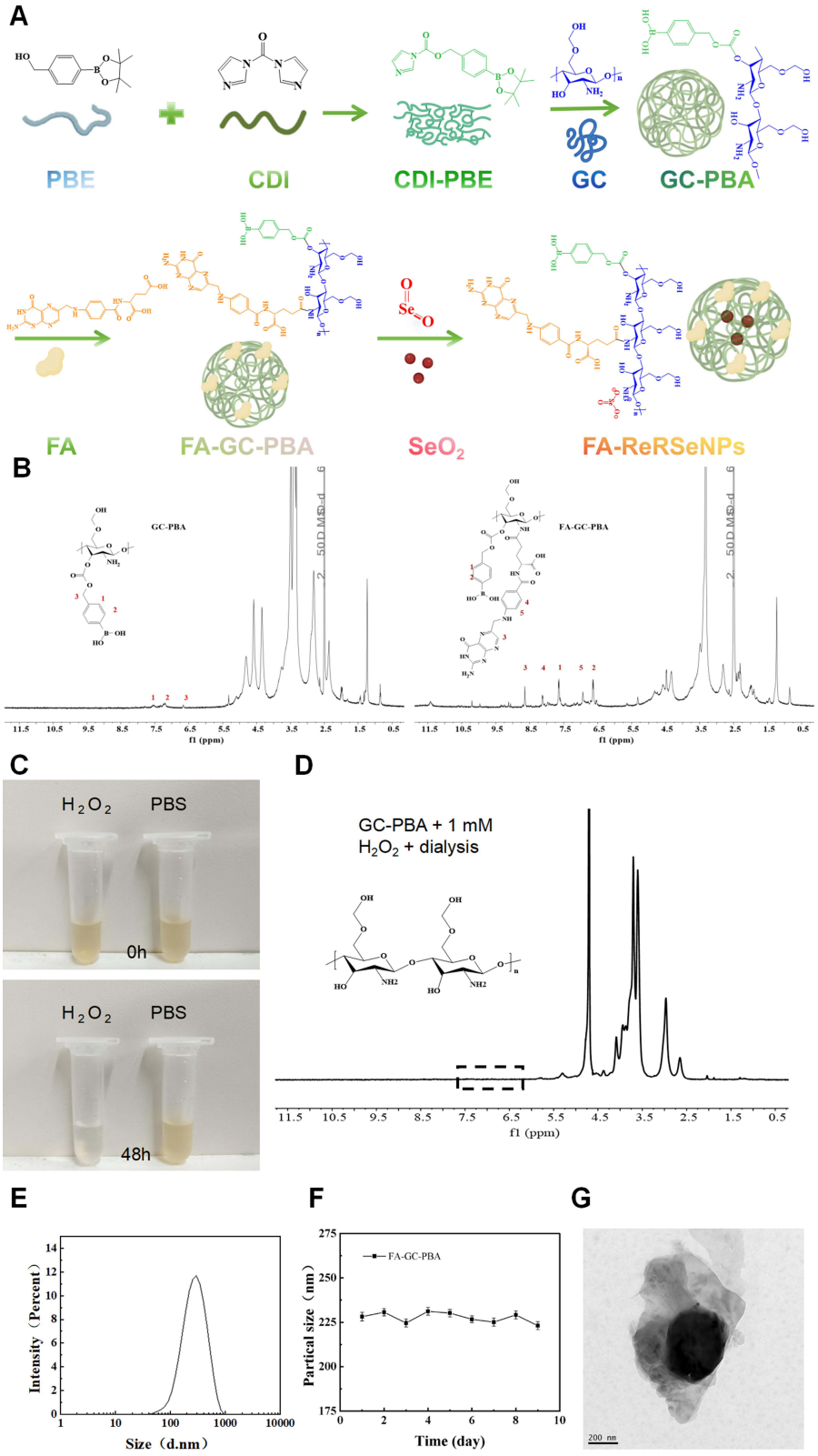

Figure 1 Synthesis and Validation of FA-ReRSeNPs. (**A**) Synthetic procedure of FA-ReRSeNPslenium. (**B**) ^{1}H NMR spectra of GC-PBA and FA-GC-PBA. (**C**) Appearance change of GC-PBA suspension before and after H_2O_2 treatment. (**D**) ^{1}H NMR spectrum of GC-PBA after H_2O_2 treatment. (**E**) Size distribution profile of FA-ReRSeNPs particles. (**F**) Stability evaluation of FA-ReRSeNPs dispersion. (**G**) Transmission electron microscopy (TEM) image of FA-ReRSeNPs (scale bar = 200 nm).

https://doi.org/10.2147/IJN.S558115

Cellular Uptake of FA-ReRSeNPs

To investigate the role of FR-mediated endocytosis in the cellular internalization of FA-ReRSeNPs, cellular uptake studies using cervical cell lines, HeLa (human cervical adenocarcinoma cell line) and SiHa (human cervical squamous cell carcinoma), expressing varying levels of FRα. Rhodamine B (RhB), encapsulated with the Se-free FA-ReRSeNPs (FA-ReRRhBNPs) for its high quantum efficiency and photo-stability, served as a fluorescent tracer for visualization by confocal laser scanning microscopy (CLSM). HeLa and SiHa cells were incubated with FA-ReRRhBNPs for 4 h at 37°C. To specifically assess FR-mediated uptake, a competitive inhibition assay was employed. Parallel samples were co-incubated with FA-ReRRhBNPs and a high concentration of free folate acid (2 mM) to saturate surface FRs. Confocal laser scanning microscopy (CLSM) imaging results showed that both HeLa and SiHa cells treated with FA-ReRRhBNPs alone exhibited strong intracellular fluorescence signals. In contrast, in the cells co - treated with FA-ReRRhBNPs and free folic acid, the intensity and distribution range of intracellular rhodamine B (RhB) fluorescence were significantly reduced (Figure 2A and B). Further quantitative statistical analysis confirmed that the difference in fluorescence signals between the two groups was statistically significant (Figure 2C and D). This significant reduction in fluorescence signal strongly indicates that free folate competitively blocked FR binding sites, thereby inhibiting the cellular internalization of the FA-ReRRhBNPs. These results provide direct evidence that visual receptor-mediated endocytosis is the primary pathway for the efficient cellular uptake of the FA-ReRRhBNPs.

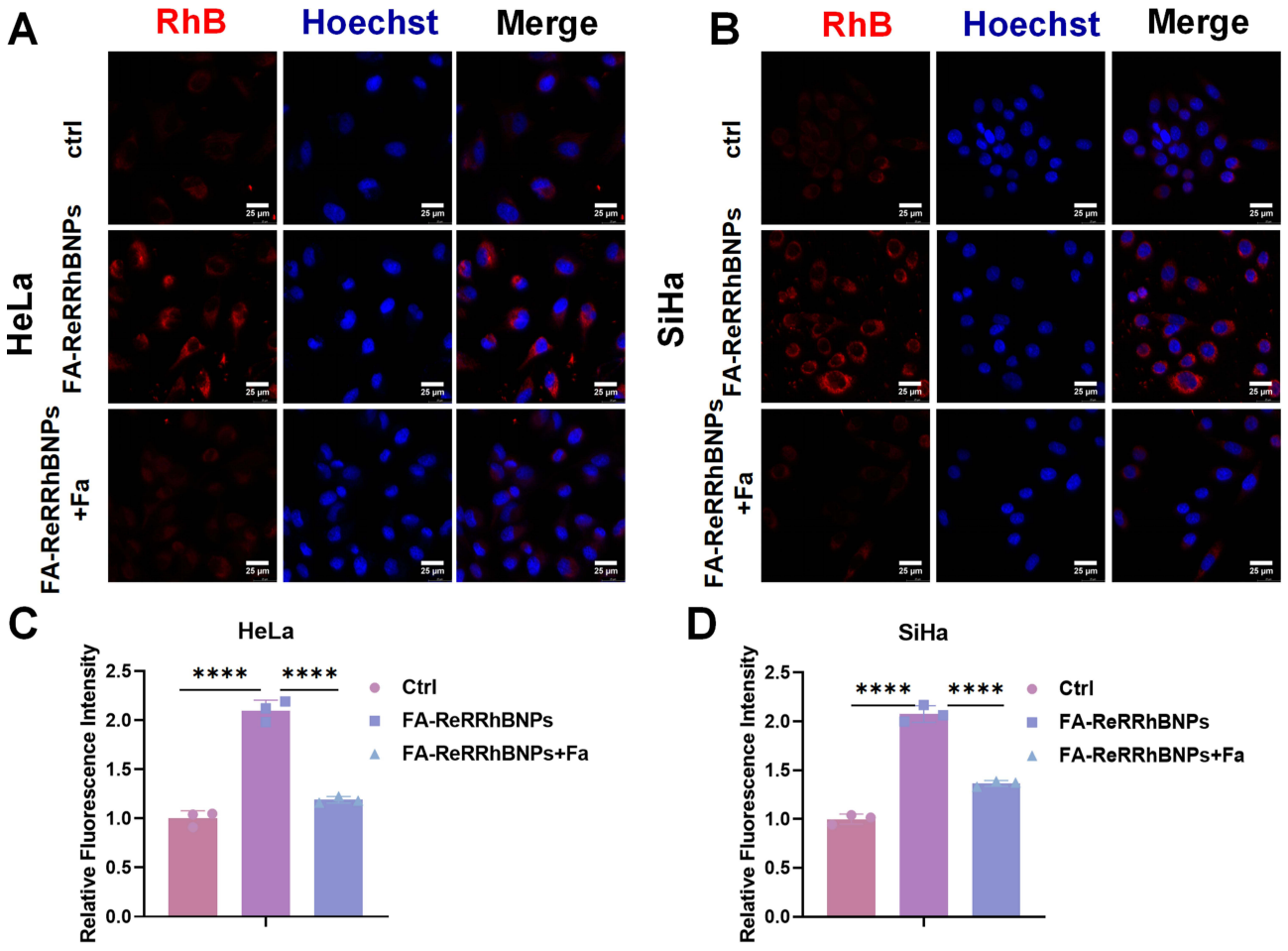

Figure 2 Cellular Uptake and Endocytosis of FA-ReRRhBNPs: (**A**) Immunofluorescence images depict the endocytosis of FA-ReRRhBNPs in HeLa cells. (**B**) Immunofluorescence images illustrate the endocytosis of FA-ReRRhBNPs in SiHa cells.(**C**) Statistical chart of A. (**D**) The statistical chart of B. FA-ReRRhBNPs are indicated by red fluorescence in the RhB channel, while cell nuclei are stained with DAPI in blue. The scale bar is 25 μm. The data is presented as mean ± SD (n=3); ****$P < 0.0001$.

https://doi.org/10.2147/IJN.S558115

FA-ReRSeNPs Inhibits Malignant Behaviors of Cervical Cancer Cells

FA-ReRSeNPs exhibited potent anticancer activity against cervical cancer cells through multiple synergistic mechanisms. As demonstrated by CCK-8 assays (Figure 3A), a 48-h treatment with FA-ReRSeNPs induced significant concentration-dependent growth inhibition, with calculated IC50 values of 1.627 μg/mL for HeLa cells and 2.746 μg/mL for SiHa cells. Colony formation assays performed at these IC50 concentrations confirmed a marked reduction in clonogenic potential (Figure 3B). Wound healing assays revealed that FA-ReRSeNPs treatment significantly delayed wound closure at 48 h (HeLa: $P<0.05$; SiHa: $P<0.001$), while no significant effect was observed at 24 h ($P>0.05$) (Figure 3C). Furthermore, Transwell migration and invasion assays demonstrated that FA-ReRSeNPs effectively suppressed both migratory ($P<0.05$) and invasive ($P<0.05$) capacities in these cell lines (Figure 3D and E).

At the molecular level (Figure 4), FA-ReRSeNPs exhibited cell type-specific cell cycle modulation: in HeLa cells, it significantly decreased the G1 phase population ($P<0.05$) while increasing S and G2/M phase fractions; in SiHa cells, it primarily reduced S phase accumulation with concomitant G2/M arrest ($P<0.05$). Western blot analysis demonstrated that these cell cycle perturbations were significantly associated with downregulation of key regulatory proteins CDK1 and Cyclin B1 (both $P<0.0001$). Additionally, Annexin V-FITC/PI double staining showed significantly increased apoptosis rates after 48-h treatment ($P<0.05$), which was mechanistically linked to upregulated pro-apoptotic BAX expression and downregulated anti-apoptotic Bcl-2 expression.

Collectively, these findings demonstrate that FA-ReRSeNPs exert anticancer effects through the following multimodal mechanisms: Concentration-dependent inhibition of cell proliferation; Significant impairment of clonogenic survival; Effective suppression of metastatic properties, including migration and invasion; Induction of cell cycle phase-specific arrest; Activation of the intrinsic apoptotic pathway.

FA-ReRSeNPs Induces Oxidative Stress in Cervical Cancer Cells and Inhibits the PI3K/AKT Signaling Pathway

Next, we explored the mechanism behind the tumor-inhibitory effects of FA-ReRSeNPs. To assess FA-ReRSeNPs's impact on oxidative stress in cervical cancer cells, we measured intracellular ROS levels using the DCFH-DA fluorescent probe and found that FA-ReRSeNPs treatment significantly increased ROS levels compared to the control group, indicating that FA-ReRSeNPs disrupts redox balance by inducing oxidative stress and causing cellular damage (Figure 5A). To systematically elucidate the key signaling pathways modulated by selenium in cervical cancer cells, we conducted comprehensive whole-transcriptome sequencing followed by bioinformatics analysis. In the volcano plot of Figure 5B, differential gene expression analysis between the Siha_SeO_2 and Siha_Ctrl groups shows 1194 significantly upregulated genes (adjusted P-value<0.05 and $\log_2$ fold change>1) and 1126 significantly downregulated genes (adjusted P-value<0.05 and $\log_2$ fold change<-1), while 27,105 genes showed no significant expression differences. Non-significant genes (blue) served as internal references, with clearly demarcated dashed lines indicating the established significance thresholds. Subsequent KEGG pathway enrichment analysis of these differentially expressed genes (Figure 5C) demonstrated that selenium treatment exerted profound modulatory effects on multiple oncogenic signaling cascades. Most remarkably, the PI3K/AKT signaling pathway exhibited the highest degree of enrichment, establishing it as the most prominently affected pathway. This finding holds particular biological significance as the PI3K/AKT axis, being a principal downstream mediator of ROS signaling, occupies a central position in governing critical cellular processes, including proliferation and apoptotic regulation in malignant cells. To validate these results, we examined the expression and phosphorylation levels of key proteins in the PI3K/AKT signaling pathway, and Western blot analysis showed that FA-ReRSeNPs treatment significantly reduced the phosphorylation levels of both PI3K and AKT in cervical cancer cells, suggesting inhibition of this pathway (Figure 5D). Together, these results indicate that the PI3K/AKT signaling pathway is central to FA-ReRSeNPs-induced apoptosis in cervical cancer cells.

FA-ReRSeNPs Significantly Inhibits Tumor Growth in vivo

Building upon our previous findings, we further evaluated the anticancer efficacy of FA-ReRSeNPs through in vivo experiments. A cervical cancer xenograft model was established by inoculating SiHa cells subcutaneously into the flanks

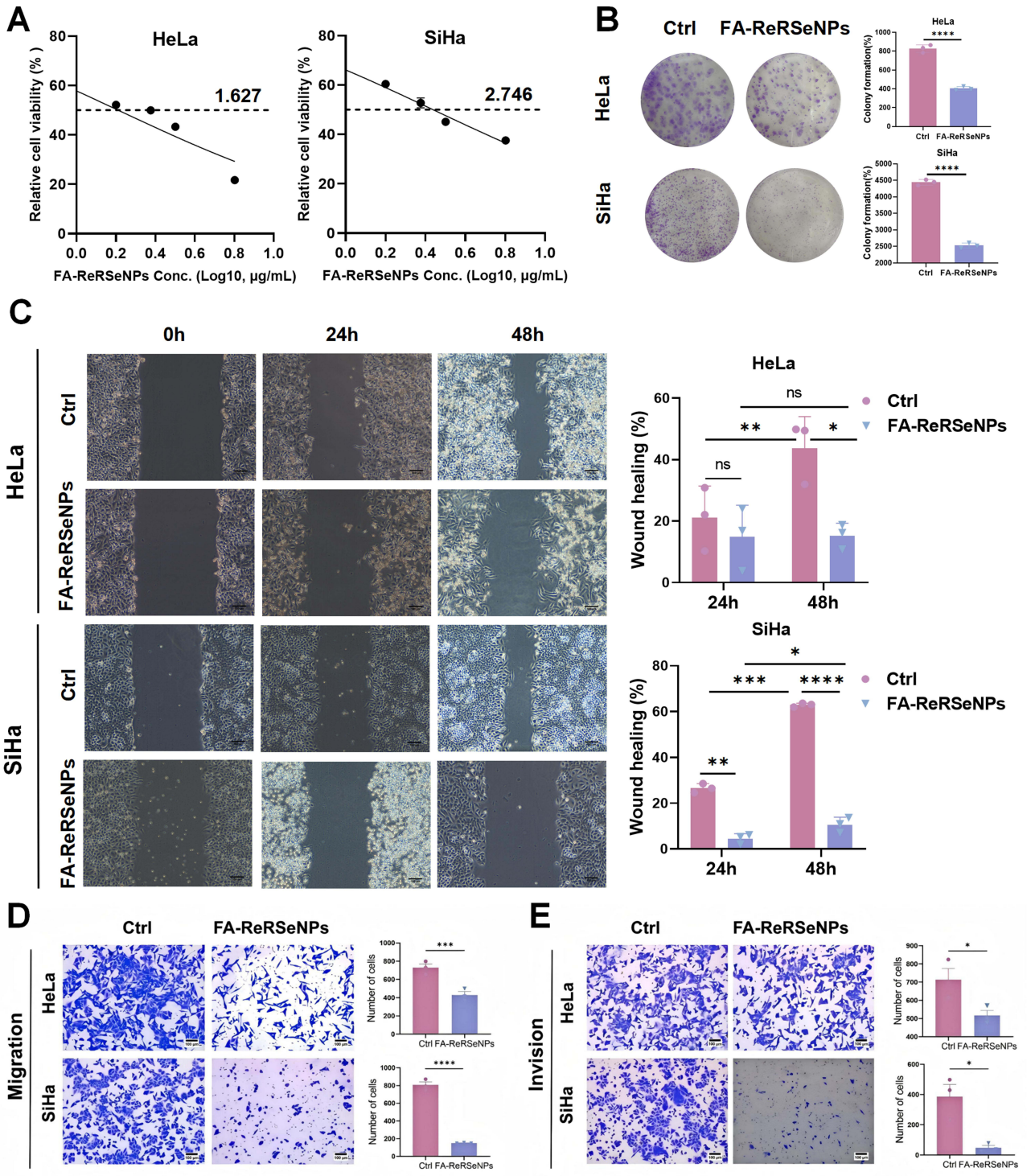

Figure 3 Anti-proliferation and anti-metastatic effects of FA-ReRSeNPs in cervical cancer cells. (**A**) CCK-8 assay demonstrating concentration-dependent inhibition of HeLa and SiHa cell proliferation following 48h treatment with FA-ReRSeNPs. Calculated IC50 values were 1.627 μg/mL for HeLa and 2.746 μg/mL for SiHa. On the proliferative capacity of HeLa and SiHa cells. (**B**) FA-ReRSeNPs suppress clonogenic potential in cervical cancer cells. Colony formation assays were conducted with HeLa (1.3 μg/mL) and SiHa (2.6 μg/mL) cells treated with FA-ReRSeNPs for 10–14 days. Quantitative analysis revealed that FA-ReRSeNPs treatment significantly inhibited colony-forming capacity in both cell lines. (**C**) Wound healing assays revealed FA-ReRSeNPs treatment inhibitory effects on the migratory capacity of HeLa and SiHa cells (scale bar = 100 μm). (**D**) Transwell chamber assays further confirmed that FA-ReRSeNPs treatment significantly inhibited cell migration (36 h). (**E**) Transwell chamber assays further confirmed that FA-ReRSeNPs treatment significantly inhibited cell invasion (48 h). Scale bar = 100 μm. Data are presented as mean ± SD (n=3); nc, $P \geq 0.05$, *$P < 0.05$, ** $P < 0.01$, ***$P < 0.001$, ****$P < 0.0001$.

https://doi.org/10.2147/IJN.S558115

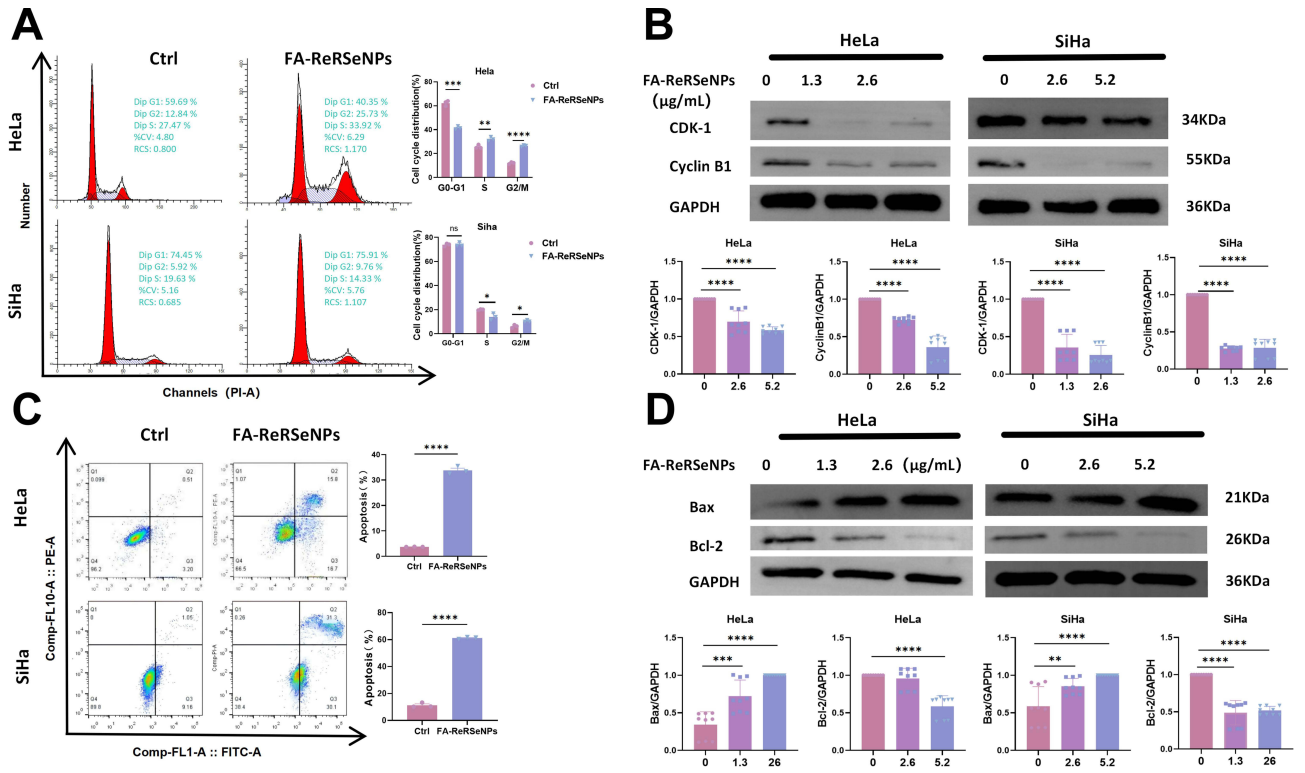

Figure 4 Effects of FA-ReRSeNPs on Cell Cycle and Apoptosis in Cervical Cancer Cells.(**A**) Cell cycle analysis of SiHa and HeLa cells following 48-h treatment with PBS or FA-ReRSeNPs. (**B**) Western blot analysis of cell cycle-related proteins in SiHa and HeLa cells after 48-h treatment with PBS or FA-ReRSeNPs. (**C**) Flow cytometry analysis of SiHa and HeLa cells post 48-h treatment with PBS or FA-ReRSeNPs. (**D**) Western blot detection of apoptosis-related proteins in SiHa and HeLa cells after 48-h treatment with PBS or FA-ReRSeNPs. GAPDH served as the internal reference protein. Data are presented as relative gray values from three independent experiments, calculated as (gray value of the target protein)/(gray value of the internal reference protein). Data represent mean ± SD (n=3); nc, $P \geq 0.05$, *$P < 0.05$, ** $P < 0.01$, ***$P < 0.001$, ****$P < 0.0001$.

of BALB/c nude mice (n=7 per group). As illustrated in Figure 6A, seven days post-cell inoculation, FA-ReRSeNPs (1.5 mg/kg) were administered via intraperitoneal injection every other day for a total of four doses (8-day treatment period). Body weight and tumor volume were monitored regularly to assess drug safety and therapeutic efficacy. The results demonstrated that all groups exhibited comparable body weight gain curves during the treatment period (Figure 6B), with no significant difference observed between the FA-ReRSeNPs and PBS control groups ($P > 0.05$), indicating the absence of apparent systemic toxicity at the tested dosage. Tumor growth analysis revealed that the FA-ReRSeNPs treatment group showed significantly reduced final tumor weight compared to the PBS control group. Notably, the nano-carrier alone group showed no statistical difference from the PBS control group ($P>0.05$), but was significantly higher than the FA-ReRSeNPs group ($P<0.05$) (Figures 6C and D). To better understand the in vivo mechanism of action, we analyzed the expression of the PI3K/AKT signaling pathway and apoptosis-related markers in tumor tissues using Western blot analysis. The results demonstrated complete consistency with the validation data obtained at the cellular level in vitro (Figure 6E and F), thus offering crucial evidence for the anti-tumor mechanism of FA-ReRSeNPs in vivo. These data clearly demonstrate that the nano-carrier itself lacks significant anticancer activity, while the encapsulated SeO_2 (Selenite) serves as the crucial active component responsible for the observed tumor growth inhibition. Histopathological examination (Figure 6G) revealed that FA-ReRSeNPs-treated mice maintained normal histological architecture in major metabolic and immune organs (liver, kidney, and spleen). The liver exhibited intact hepatic cord architectures, accompanied by well-demarcated lobular structures with clear organizational boundaries, while the kidney showed preserved glomerular and tubular morphology. The spleen demonstrated distinct demarcation between red and white pulp. These findings indicate that FA-ReRSeNPs administration at the experimental dosage did not induce significant organ toxicity. Of particular importance, histological analyses revealed no drug-related pathological alterations in the liver (primary metabolic organ) and kidneys (major excretory organs), directly validating the

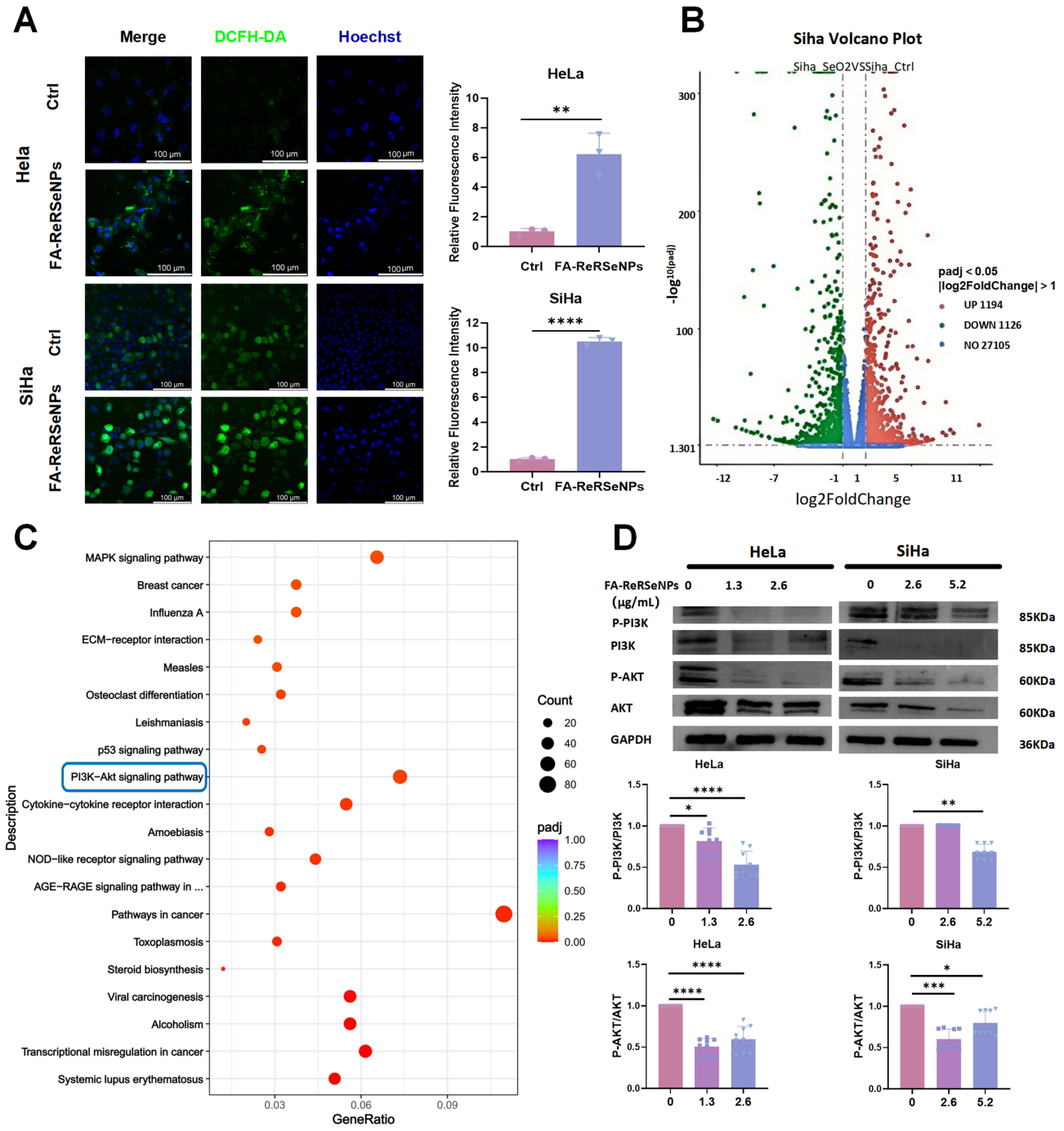

Figure 5 FA-ReRSeNPs inhibit the PI3K/AKT signaling pathway in cervical cancer cells by inducing oxidative stress. (**A**) Intracellular ROS levels in HeLa and SiHa cells treated with FA-ReRSeNPs were measured using the DCFH-DA fluorescent probe (scale bars: HeLa = 100 μm, SiHa = 100 μm). (**B**) Volcano plot displays the distribution of differentially expressed genes (DEGs). (**C**) KEGG pathway analysis (bubble chart) demonstrates statistically significant enrichment of signaling pathways associated with differentially expressed genes (DEGs) related to SiHa cell growth, with the target signaling pathway selected for this study highlighted by the blue box. (**D**) Western blot analysis demonstrated the inhibitory effect of FA-ReRSeNPs on key proteins in the PI3K/AKT signaling pathway, GAPDH served as the internal reference protein. Data are presented as relative gray values from three independent experiments, calculated as (gray value of the target protein)/(gray value of the internal reference protein). Data are presented as mean ± SD (n=3); **P* < 0.05, ** *P* < 0.01, ****P* < 0.001, *****P* < 0.0001.

favorable biosafety profile of FA-ReRSeNPs. Furthermore, the spleen, a central immune organ, preserved its native tissue architecture, which implies that this nanotherapeutic does not elicit detectable immunotoxicity at the tested concentration. Collectively, these outcomes robustly demonstrate the in vivo safety superiority of FA-ReRSeNPs, laying a solid foundation for their potential clinical translation.

https://doi.org/10.2147/IJN.S558115

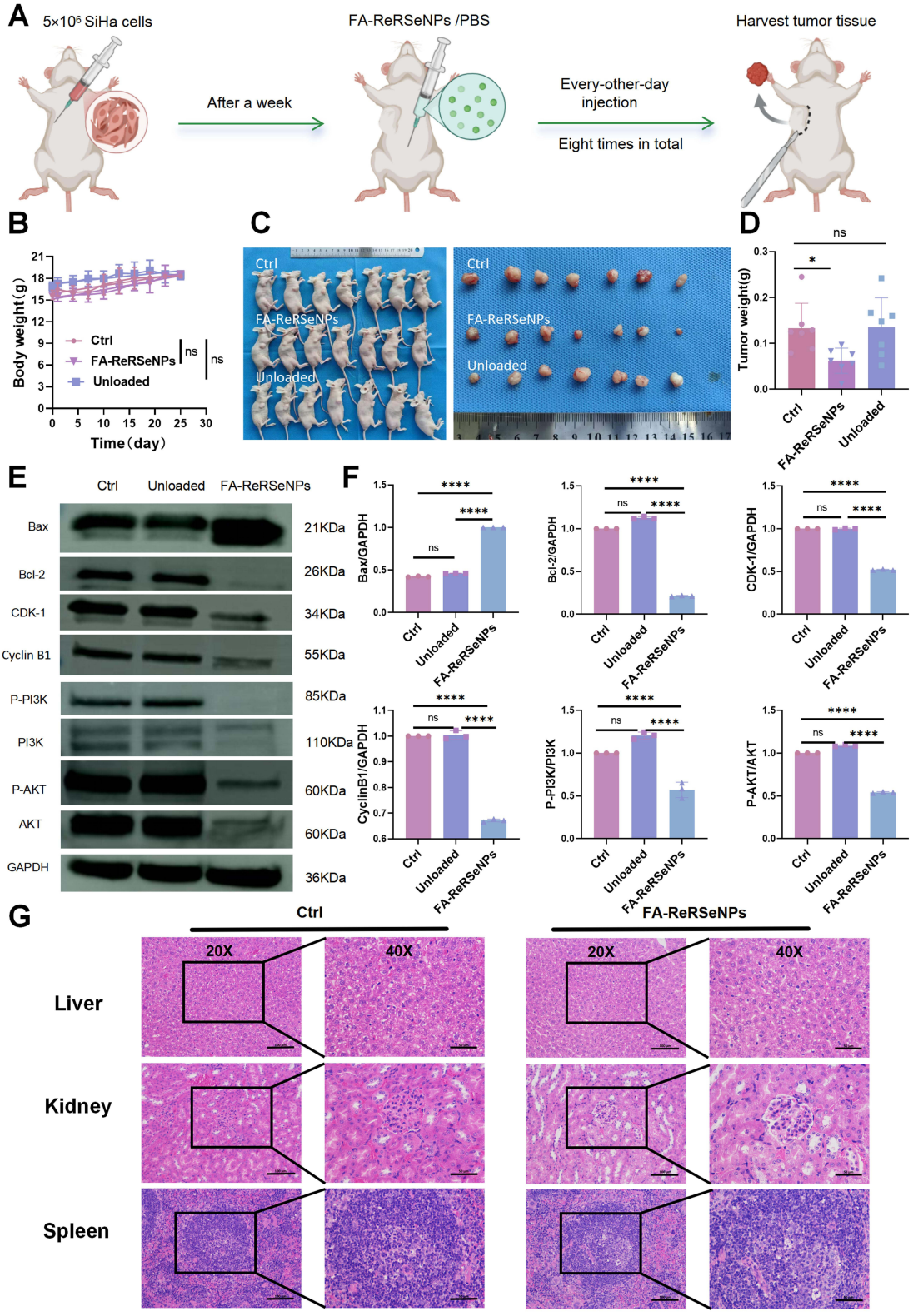

Figure 6 FA-ReRSeNPs demonstrate strong anticancer activity in vivo. (**A**) Schematic of the experimental protocol. (**B**) Longitudinal body weight profiles for control, FA-ReRSeNP-treated, and unloaded groups over the study period. (**C**) Gross images of mice from each group and of resected subcutaneous xenograft tumors. (**D**) Comparison of tumor weights across treatment groups. (**E**) Western blotting for proteins related to cell cycle, apoptosis, and the PI3K/AKT signaling pathway in tumor tissue extracts, GAPDH served as the internal reference protein. Data are presented as relative gray values from three independent experiments, calculated as (gray value of the target protein)/(gray value of the internal reference protein). (**F**) Quantification of the data shown in panel. (**G**) Hematoxylin–eosin (HE) staining of mouse liver, kidney, and spleen (scale bar = 50 μm at 20×; scale bar = 100 μm at 40×). Data are mean ± SD (n=3); nc, $P \geq 0.05$; *$P < 0.05$; ****$P < 0.0001$.

https://doi.org/10.2147/IJN.S558115

Discussion

Cervical cancer disproportionately affects populations in impoverished regions, necessitating the development of safe, effective, and logistically feasible therapeutic options that are low-cost and stable during storage/transport. Se, an essential trace element, poses challenges due to its narrow therapeutic window-high doses may harm normal cells. A key strategy to mitigate systemic toxicity is to enhance Se accumulation in tumor sites while enabling controlled release.

Our previous studies demonstrated that while SeO_2 exhibits growth inhibitory effects on cervical cancer cells in both in vitro and animal models, its clinical application has been substantially limited by the requirement for high therapeutic doses and the potential for hepatorenal toxicity during prolonged administration. To address these critical limitations, we have innovatively developed FA-ReRSeNPs. Comprehensive in vitro and in vivo evaluations revealed that FA-ReRSeNPs exert potent anticancer effects through multiple mechanisms at significantly reduced dosages, including: (i) activation of apoptotic pathways, (ii) remarkable suppression of tumor cell migration and invasion, and (iii) effective blockade of cell cycle progression. Most notably, in BALB/c nude mouse xenograft models, FA-ReRSeNPs treatment achieved significant tumor growth inhibition without inducing observable toxic side effects, demonstrating an exceptional efficacy-safety profile that strongly supports its clinical translation potential.

The ROS-responsive property of FA-ReRSeNPs is central to its anticancer activity. Cancer cells exhibit heightened metabolic activity, leading to elevated ROS in the tumor microenvironment (TME).[34] FA-ReRSeNPs is engineered to release Se specifically in high-ROS environments, disrupting redox balance and inducing apoptosis. Experimental data showed that FA-ReRSeNPs treatment increased intracellular ROS levels in cervical cancer cells, accompanied by cell cycle perturbations, upregulation of pro-apoptotic Bax, and downregulation of anti-apoptotic Bcl-2. These findings indicate that FA-ReRSeNPs exacerbate oxidative stress to drive cancer cell death.

The PI3K/AKT signaling pathway is critical for cervical cancer progression,[35] with its hyperactivation linked to cell proliferation, survival, and metastasis.[36] FA-ReRSeNPs significantly inhibited PI3K and AKT phosphorylation, blocking pathway activation. Mechanistic studies revealed that FA-ReRSeNPs downregulated downstream effectors (eg, MDM2, NF-kappa B) via PI3K/AKT inhibition, ultimately suppressing cell proliferation and promoting apoptosis. These results identify PI3K/AKT as a key molecular target for FA-ReRSeNPs's anticancer effects.

The FA-ReRSeNPs system achieves precise targeting of the tumor microenvironment (TME) through two mechanisms: first, ROS-responsive drug release, which leverages the elevated ROS levels in the TME to intelligently release active selenium within cancer cells, thereby reducing toxicity to normal tissues and enhancing targeting precision; second, FA-ReRSeNPs realize precise targeting of cervical cancer cells through the specific binding between the folate molecules they carry and the highly expressed folate receptors on the surface of tumor cells, and then exert anti-tumor effects. FA-ReRSeNPs induce tumor cell apoptosis through multiple synergistic pathways: oxidative stress-mediated cytotoxicity (elevated intracellular ROS levels disrupt redox homeostasis, leading to DNA damage and mitochondrial dysfunction); PI3K/AKT pathway inhibition (downregulation of this pathway suppresses proliferation and promotes apoptosis, as evidenced by changes in the Bcl-2/Bax ratio); and improved drug delivery (the nanocarrier enhances tumor accumulation and bioavailability compared to free selenium compounds).

Despite the phased achievements in elucidating the synergistic targeting mechanism and therapeutic efficacy of our selenium-based nanosystem, a number of limitations require further exploration and mitigation in future studies. First, a systematic and in-depth evaluation of the in vivo pharmacokinetic characteristics of FA-ReRSeNPs has not been performed. The absorption efficiency, tissue distribution pattern, metabolic transformation pathway, and excretion and clearance mechanisms of FA-ReRSeNPs within the organism are still unclear. This lack of clarity may hinder accurate scientific assessments of the formulation's bioavailability, duration of action, and targeting delivery precision. Second, there is insufficient systematic data regarding long-term toxicity. Current short-term safety evaluations only reflect the safety characteristics of the formulation under acute or sub-acute exposure. Consequently, they do not comprehensively address the potential risks associated with long-term clinical applications. Critical issues such as organ accumulation toxicity, chronic inflammatory responses, and the induction of immunogenicity require further investigation. Third, the therapeutic efficacy of this formulation in immunocompetent models has not been thoroughly validated. Most existing

studies utilize immunodeficient models, which do not accurately replicate the complex tumor immune microenvironment found in clinical patients. This limitation may introduce biases in evaluating the therapeutic effects and obscure the formulation's true therapeutic potential in clinical practice.

Despite the aforementioned deficiencies, the FA-ReRSeNPs nanoplatform has demonstrated significant potential for clinical translation. It has shown targeted enrichment ability and excellent anticancer activity, and it causes no obvious damage to the main organs (liver and kidney). As an efficient targeted delivery platform, it can be combined with traditional chemotherapeutic drugs such as cisplatin or novel anticancer drugs such as immune checkpoint inhibitors. It is expected to further improve the therapeutic effect and reduce the side effects of single-drug treatment through a synergistic mechanism, providing new ideas and strategies for the precise treatment of cervical cancer.

Conclusion

This study shows that FA-ReRSeNPs robustly inhibit cervical cancer cell growth and proliferation in both in vitro and in vivo models. The primary mechanisms include suppression of the PI3K/AKT signaling pathway, induction of cancer cell apoptosis, and inhibition of tumor invasion and metastasis. The formulation demonstrated excellent biocompatibility, potent anticancer activity, and low toxicity toward normal cells, supporting its further clinical development for cervical cancer therapy. Future work will concentrate on optimizing the nanoparticle formulation. By precisely adjusting carrier ratios, refining surface modification techniques, and improving particle size control, we aim to enhance the stability, biocompatibility, and targeted delivery efficiency of the preparation. Given the high expression of folate receptors in various solid tumors, including ovarian, breast, and lung cancers, we will extend targeted therapy studies to evaluate the preparation's broad-spectrum anticancer potential. Subsequent studies will also prioritize dosage-form optimization, comprehensive safety assessment, and investigation of combination-therapy regimens. Systematic pharmacokinetic and long-term toxicity data will be collected to support the clinical translation of this preparation.

Abbreviations

AKT(PKB), Protein Kinase B; Bax, Bcl-2 associated X protein; BCA, Bicinchoninic Acid Assay; Bcl-2, B-cell lymphoma/Leukemia-2; CDI, 1,1'-Carbonyldiimidazole; CDK1, Cyclin-dependent kinase 1; CCK-8, Cell Counting Kit-8; CLSM, confocal laser scanning microscopy; DCM, Dichloromethane; DMSO, Dimethyl sulfoxide; EE, entrapment efficiency; DEGs, differentially expressed genes; GO, Gene Ontology; EDC·HCl, N-(3-Dimethylaminopropyl)-N'-ethylcarbodiimide hydrochloride; FA, folic acid; FRs, folate receptors; FA-ReRSeNPs, engineered novel ROS-responsive selenium nanoparticles; GAPDH, Glyceraldehyde-3-phosphate dehydrogenase; GC, Glycol Chitosan; HE staining, Hematoxylin–eosin staining; HPV, Human papillomavirus; ICP-OES, Inductively Coupled Plasma Optical Emission Spectrometry; IC50, Half-maximal inhibitory concentration; LE, loading efficiency; NHS, N-Hydroxysuccinimide; OD, optical density; IC50, Half Maximal Inhibitory Concentration; PBE, 4-(Hydroxymethyl)phenylboronic acid pinacol ester; PBS, Phosphate-buffered saline; PI3K, Phosphoinositide 3-Kinase; PVDF, Polyvinylidene Fluoride; RhB, Rhodamine B; ROS, Reactive oxygen species; RNA, Ribonucleic Acid; Se, Selenium; SeO_2, Selenium dioxide; H_2SeO_3, selenous acid; SeO_3^{2-}, Selenite anion; SDS-PAGE, Sodium Dodecyl Sulfate-Polyacrylamide Gel Electrophoresis; SPF, specific pathogen-free; TEM, Transmission electron microscopy; TBST, Tris-Buffered Saline with Tween® 20.

Data Sharing Statement

The data that support the findings of this study are available from the corresponding author, Dr. Fei Guo, upon reasonable request. Please contact via Email at guofei2005@126.com or lhlguofei@nbu.edu.cn.

Ethics Approval and Consent to Participate

All animal experiments were conducted under the guidance of the Experimental Animal Welfare and Ethics Committee of Ningbo Life and Health Industry Research Institute, Chinese Academy of Sciences (Approval No.: GK-2023-06-0001). This animal use protocol has been reviewed and approved by the Institutional Animal Care and Use Committee (IACUC), in compliance with GB/T 35892-2018 "Guidelines for Ethical Review of Experimental Animal Welfare".

Author Contributions

All authors made a significant contribution to the work reported, whether that is in the conception, study design, execution, acquisition of data, analysis and interpretation, or in all these areas; took part in drafting, revising or critically reviewing the article; gave final approval of the version to be published; have agreed on the journal to which the article has been submitted; and agree to be accountable for all aspects of the work.

Funding

This work is supported by the following projects: the National Natural Science Foundation of China (Grant No. 81972445) and the Science and Technology Innovation Key R&D Program of "Kechuang Yongjiang 2035" R&D Program (025Z174).

Disclosure

The authors declare that they have no competing interests during this work.

References

1. Rayner M, Welp A, Stoler MH, Cantrell LA. Cervical cancer screening recommendations: now and for the future. *Healthcare*. 2023;11(16):2273. doi:10.3390/healthcare11162273
2. Li Z, Liu P, Yin A, et al. Global landscape of cervical cancer incidence and mortality in 2022 and predictions to 2030: the urgent need to address inequalities in cervical cancer. *Int J Cancer*. 2025;157(2):288–297. doi:10.1002/ijc.35369
3. Drolet M, Bénard É, Pérez N, Brisson M. Population-level impact and herd effects following the introduction of human papillomavirus vaccination programmes: updated systematic review and meta-analysis. *Lancet*. 2019;394(10197):497–509. doi:10.1016/S0140-6736(19)30298-3
4. Rahangdale L, Mungo C, O'Connor S, Chibwesha CJ, Brewer NT. Human papillomavirus vaccination and cervical cancer risk. *BMJ*. 2023;383:p2901. doi:10.1136/bmj.p2901
5. Tewari KS, Sill MW, Penson RT, et al. Bevacizumab for advanced cervical cancer: final overall survival and adverse event analysis of a randomised, controlled, open-label, Phase 3 trial (Gynecologic Oncology Group 240). *Lancet*. 2017;390(10103):1654–1663. doi:10.1016/S0140-6736(17)31607-0
6. Kuršvietienė L, Mongirdienė A, Bernatonienė J, Šulinskienė J, Stanevičienė I. Selenium anticancer properties and impact on cellular redox status. *Antioxidants*. 2020;9(1):80. doi:10.3390/antiox9010080
7. Stolwijk JM, Garje R, Sieren JC, Buettner GR, Zakharia Y. Understanding the redox biology of selenium in the search of targeted cancer therapies. *Antioxidants*. 2020;9(5):420. doi:10.3390/antiox9050420
8. Minich WB. Selenium metabolism and biosynthesis of selenoproteins in the human body. *Biochem Biokhimiia*. 2022;87(Suppl 1):S168–s102. doi:10.1134/S0006297922140139
9. Steinbrenner H, Duntas LH, Rayman MP. The role of selenium in type-2 diabetes mellitus and its metabolic comorbidities. *Redox Biol*. 2022;50:102236. doi:10.1016/j.redox.2022.102236
10. Leiter O, Zhuo Z, Rust R, et al. Selenium mediates exercise-induced adult neurogenesis and reverses learning deficits induced by hippocampal injury and aging. *Cell Metab*. 2022;34(3):408–423.e408. doi:10.1016/j.cmet.2022.01.005
11. Hariharan S, Dharmaraj S. Selenium and selenoproteins: it's role in regulation of inflammation. *Inflammopharmacology*. 2020;28(3):667–695. doi:10.1007/s10787-020-00690-x
12. Lee KH, Jeong D. Bimodal actions of selenium essential for antioxidant and toxic pro-oxidant activities: the selenium paradox (Review). *Mol Med Rep*. 2012;5(2):299–304. doi:10.3892/mmr.2011.651
13. Selenius M, Rundlöf AK, Olm E, Fernandes AP, Björnstedt M. Selenium and the selenoprotein thioredoxin reductase in the prevention, treatment and diagnostics of cancer. *Antioxid Redox Signaling*. 2010;12(7):867–880. doi:10.1089/ars.2009.2884
14. Misra S, Boylan M, Selvam A, Spallholz JE, Björnstedt M. Redox-active selenium compounds--from toxicity and cell death to cancer treatment. *Nutrients*. 2015;7(5):3536–3556. doi:10.3390/nu7053536
15. Razaghi A, Zickler AM, Spallholz J, Kirsch G, Björnstedt M. Selenofolate inhibits the proliferation of IGROV1 cancer cells independently from folate receptor alpha. *Heliyon*. 2021;7(6):e07254. doi:10.1016/j.heliyon.2021.e07254
16. Chen D, Cai B, Zhu Y, et al. Targeting histone demethylases JMJD3 and UTX: selenium as a potential therapeutic agent for cervical cancer. *Clin Epigenetics*. 2024;16(1):51. doi:10.1186/s13148-024-01665-3
17. Liu T, Xu L, He L, et al. Selenium nanoparticles regulates selenoprotein to boost cytokine-induced killer cells-based cancer immunotherapy. *Nano Today*. 2020;35:100975. doi:10.1016/j.nantod.2020.100975
18. Song Z, Luo W, Zheng H, Zeng Y, Wang J, Chen T. Translational nanotherapeutics reprograms immune microenvironment in malignant pleural effusion of lung adenocarcinoma. *Adv Healthcare Mater*. 2021;10(12):e2100149. doi:10.1002/adhm.202100149
19. Liu C, Lai H, Chen T. Boosting natural killer cell-based cancer immunotherapy with selenocystine/transforming growth factor-beta inhibitor-encapsulated nanoemulsion. *ACS Nano*. 2020;14(9):11067–11082. doi:10.1021/acsnano.9b10103
20. Collery P. Strategies for the development of selenium-based anticancer drugs. *J Trace Elements Med Biol*. 2018;50:498–507. doi:10.1016/j.jtemb.2018.02.024
21. Liu C, Ding L, Bai L, et al. Folate receptor alpha is associated with cervical carcinogenesis and regulates cervical cancer cells growth by activating ERK1/2/c-Fos/c-Jun. *Biochem Biophys Res Commun*. 2017;491(4):1083–1091. doi:10.1016/j.bbrc.2017.08.015
22. Yazaki S, Kojima Y, Yoshida H, et al. High expression of folate receptor alpha is associated with poor prognosis in patients with cervical cancer. *J Gynecolog Oncol*. 2022;33(6):e82. doi:10.3802/jgo.2022.33.e82

23. Saito A, Nishikawa T, Yoshida H, et al. Folate receptor alpha expression is widely observed in uterine and ovarian carcinosarcoma (209). *Gynecologic Oncol*. 2022;166:S116–S117.
24. Weinberg F, Ramnath N, Nagrath D. Reactive oxygen species in the tumor microenvironment: an overview. *Cancers*. 2019;11(8). doi:10.3390/cancers11081191
25. Aboelella NS, Brandle C, Kim T, Ding ZC, Zhou G. Oxidative stress in the tumor microenvironment and its relevance to cancer immunotherapy. *Cancers*. 2021;13(5):986. doi:10.3390/cancers13050986
26. Xu Z, Fan R, Zhang X, et al. Regulation of ROS balance in the tumor microenvironment achieves reversal of immune suppression and deep penetration of nanomedicines. *Chem Eng J*. 2025;505:159716. doi:10.1016/j.cej.2025.159716
27. Yassein AS, Elamary RB, Alwaleed EA. Biogenesis, characterization, and applications of Spirulina selenium nanoparticles. *Microb Cell Fact*. 2025;24(1):39. doi:10.1186/s12934-025-02656-6
28. Broaders KE, Grandhe S, Fréchet JM. A biocompatible oxidation-triggered carrier polymer with potential in therapeutics. *J Am Chem Soc*. 2011;133(4):756–758. doi:10.1021/ja110468v
29. Lv W, Xu J, Wang X, Li X, Xu Q, Xin H. Bioengineered boronic ester modified dextran polymer nanoparticles as reactive oxygen species responsive nanocarrier for ischemic stroke treatment. *ACS nano*. 2018;12(6):5417–5426. doi:10.1021/acsnano.8b00477
30. Niu L, Zhu F, Li B, et al. Folate-conjugated and pH-triggered doxorubicin and paclitaxel co-delivery micellar system for targeted anticancer drug delivery. *Mater Chem Front*. 2018;2(8):1529–1538. doi:10.1039/C8QM00217G
31. Jing C, Chen S, Bhatia SS, et al. Bone-targeted polymeric nanoparticles as alendronate carriers for potential osteoporosis treatment. *Polym Test*. 2022;110:107584. doi:10.1016/j.polymertesting.2022.107584
32. Yamani JS, Lounsbury AW, Zimmerman JB. Adsorption of selenite and selenate by nanocrystalline aluminum oxide, neat and impregnated in chitosan beads. *Water Res*. 2014;50:373–381. doi:10.1016/j.watres.2013.10.054
33. Shen C, Zhao L, Du X, et al. Smart responsive quercetin-conjugated glycol chitosan prodrug micelles for treatment of inflammatory bowel diseases. *Mol Pharmaceut*. 2021;18(3):1419–1430. doi:10.1021/acs.molpharmaceut.0c01245
34. Schieber M, Chandel NS. ROS function in redox signaling and oxidative stress. *Current Biol*. 2014;24(10):R453–462. doi:10.1016/j.cub.2014.03.034
35. Nayim P, Mbaveng AT, Sanjukta M, Rikesh J, Kuete V, Sudhir K. CD24 gene inhibition and TIMP-4 gene upregulation by Imperata cylindrica's root extract prevents metastasis of CaSki cells via inhibiting PI3K/Akt/snail signaling pathway and blocking EMT. *J Ethnopharmacol*. 2021;275:114111. doi:10.1016/j.jep.2021.114111
36. Glaviano A, Foo ASC, Lam HY, et al. PI3K/AKT/mTOR signaling transduction pathway and targeted therapies in cancer. *Mol Cancer*. 2023;22(1):138. doi:10.1186/s12943-023-01827-6